

AD-A087 738

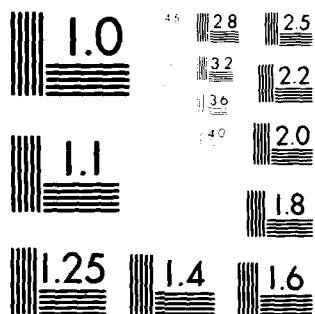
ARMY ELECTRONICS RESEARCH AND DEVELOPMENT COMMAND WS--ETC F/6 17/5
ON THE FEASIBILITY OF USING FLIR (FORWARD LOOKING INFRARED) DAT--ETC(U)
JUN 80 G R OCHS, S F CLIFFORD, T WANG
ERADCOM/ASL-CR-80-8003-1

UNCLASSIFIED

NL

1 of 1
AD-A
CR-80-8003-1

END
DATE
FILMED
9-80
DTIC



MICROCOPY RESOLUTION TEST CHART
 NATIONAL BUREAU OF STANDARDS-1963-A

LEVEL

12

ASL-CR-80-8003-1

AD

Reports Control Symbol
OSD-1366

ADA 087738

ON THE FEASIBILITY OF USING FLIR (FORWARD LOOKING INFRARED)
DATA FOR CROSSWIND MEASUREMENTS

JUNE 1980

DTIC
C O C T E
AUG 11 1980
C

Prepared by

G. R. Ochs
S. F. Clifford
Ting-i Wang

NOAA/ERL/Wave Propagation Laboratory
Boulder, Colorado 80303

ASL Project Order 79-8003

Monitor: William J. Vechione

Approved for public release; distribution unlimited



US Army Electronics Research and Development Command
ATMOSPHERIC SCIENCES LABORATORY
White Sands Missile Range, NM 88002

DDC FILE COPY

80 8 8 006

NOTICES

Disclaimers

The findings in this report are not to be construed as an official Department of the Army position, unless so designated by other authorized documents.

The citation of trade names and names of manufacturers in this report is not to be construed as official Government indorsement or approval of commercial products or services referenced herein.

Disposition

Destroy this report when it is no longer needed. Do not return it to the originator.

14 ERADZOM/ASL-CE-8003-1

SECURITY CLASSIFICATION OF THIS PAGE (When Data Entered)

REPORT DOCUMENTATION PAGE		READ INSTRUCTIONS BEFORE COMPLETING FORM
1. RECIPIENT'S CATALOG NUMBER ASL-CE-8003-1	2. GOVT ACCESSION NO. AD-A087138	3. RECIPIENT'S CATALOG NUMBER
4. TITLE (and Subtitle) ON THE FEASIBILITY OF USING FLIR (FORWARD LOOKING INFRARED) DATA FOR CROSSWIND MEASUREMENTS		5. TYPE OF REPORT & PERIOD COVERED R&D Technical Report
7. AUTHOR(s) G. R. Ochs, S. F. Clifford, Ting-i Wang		6. PERFORMING ORG. REPORT NUMBER
9. PERFORMING ORGANIZATION NAME AND ADDRESS NOAA/ERL/Wave Propagation Laboratory Boulder, Colorado 80303		8. CONTRACT OR GRANT NUMBER(s) ASL Project Order 79-8003
11. CONTROLLING OFFICE NAME AND ADDRESS US Army Electronics Research and Development Command Adelphi, MD 20783		10. PROGRAM ELEMENT, PROJECT, TASK AREA & WORK UNIT NUMBERS DA Task 1L162111AH71-24
14. MONITORING AGENCY NAME & ADDRESS (if different from Controlling Office) Atmospheric Sciences Laboratory White Sands Missile Range, NM 88002		12. REPORT DATE June 1980
		13. NUMBER OF PAGES 45
		15. SECURITY CLASS. (of this report) UNCLASSIFIED
		15a. DECLASSIFICATION/DOWNGRADING SCHEDULE
16. DISTRIBUTION STATEMENT (of this Report) Approved for public release; distribution unlimited.		
17. DISTRIBUTION STATEMENT (of the abstract entered in Block 20, if different from Report)		
18. SUPPLEMENTARY NOTES ASL Monitor: William J. Vechione		
19. KEY WORDS (Continue on reverse side if necessary and identify by block number) Crosswinds Weighting function Forward looking infrared Covariance Scintillation Feasibility study		
20. ABSTRACT (Continue on reverse side if necessary and identify by block number) In this report, we theoretically examine, and experimentally test the feasibility of extracting crosswind information from a forward looking infrared thermal sight system (FLIR). A general solution to the problem of obtaining crosswind information from the observation of focal plane image fluctuations is obtained. Wind weighting functions are obtained for receiving apertures and detector sizes of interest for the particular case of viewing the horizon. Experimental results are presented from measurements at visible		

DD FORM 1 JAN 73 1473

EDITION OF 1 NOV 65 IS OBSOLETE

420663
SECURITY CLASSIFICATION

When Data Entered

20. ABSTRACT (cont)

C sub n to the 2nd power
wavelengths using stationary detectors placed in the focal plane, and also from the recorded video signals obtained directly from the FLIR. These results show that under controlled conditions with a suitable scene and level it is possible to obtain crosswind information from the FLIR system provided that:

1. C_n^2 is greater than about $1 \times 10^{-14} \text{ m}^{2/3}$
2. There is sufficient contrast of the right kind in the image
3. The thermal sight is stationary
4. The thermal sight image is in exact focus
5. Wind speeds are less than 4 m/s

CONTENTS

1. INTRODUCTION.....	5
2. THEORY OF WIND MEASUREMENT BY OBSERVATION OF IMAGE FLUCTUATIONS.....	6
3. EXPERIMENTAL MEASUREMENTS.....	18
3.1 Wind Measurements at Visual Wavelengths.....	18
3.2 Wind Measurements from FLIR Thermal Sight Signals.....	25
4. CONCLUSIONS AND RECOMMENDATIONS.....	41
5. REFERENCES.....	45

Accession For	
NR15 CEN&I	<input checked="checked" type="checkbox"/>
ENC TAB	<input type="checkbox"/>
1. Summary and	
2. Description of	
3. Objectives	
4. Results	
5. Conclusions	
6. Recommendations	
7. Other	
8. Remarks	
9. Signature	
10. Date	

A

1. INTRODUCTION

We report here the results of a study of the feasibility of measuring crosswinds by observing fluctuations in the image formed by a lens observing an arbitrary scene. The study is especially concerned with observations in the 10 μm wavelength region used by the FLIR thermal sight system, and how this passive system might be used to obtain crosswind information. This report is submitted to fulfill the requirements of Project Order ASL798003 issued by the U. S. Army Electronics Command, Atmospheric Sciences Laboratory, White Sands Missile Range, New Mexico.

A previous report¹ discussed the feasibility of measuring crosswinds by observing the scintillation of the natural background radiation. The analysis technique was that used for previous passive wind sensing devices operating at visible wavelengths. A new theoretical development is required to understand the origin of image plane fluctuations. The theory, presented in the next section, is compared quantitatively with data obtained from two experiments. Additional quantitative comparisons which involve extensive computer calculations will be available in a future publication.

In one experiment, we made continuous observations of crosswinds at visible wavelengths in real time; in the other, tape recorded electrical signals from the FLIR instrument were analyzed. Both experiments were conducted over the same 500 m test range. The visible wavelength experiment was conducted under more favorable conditions than the FLIR experiment and the simpler test arrangement was easier to analyze. The FLIR analysis was complicated because it uses a system with intermittent sampling, and has other problems, but actual use of the instrument was extremely helpful in understanding the practical difficulties of adding an optical crosswind capability to this instrument.

2. THEORY OF WIND MEASUREMENT BY OBSERVATION OF IMAGE FLUCTUATIONS

We can analyze the FLIR problem using the classical Huygen-Fresnel (H-F) approach: Figure 1 illustrates a scene $u_1(\rho_1)$ a distance away from a lens which images the scene a distance $f + \delta$ in back of the lens. The image $u_i(\rho)$ is given by

$$u_i(\rho) = \frac{-ik}{2\pi(f + \delta)} e^{\frac{ik\rho^2}{2(f + \delta)} + ik(f + \delta)} \int d^2\rho_2 u_3(\rho_2) e^{\frac{ik\rho_2^2}{2(f + \delta)} - \frac{ik\rho_2 \cdot \rho}{(f + \delta)}} \quad (1)$$

The field $u_3(\rho_2)$ is related to the field incident upon the lens $u_2(\rho_2)$ by the lens transfer function

$$u_3(\rho_2) = u_2(\rho_2) e^{-ik\rho_2^2/2f} W(\rho_2) \quad (2)$$

where W is the aperture weighting function, assumed Gaussian, $W(\rho_2) = \exp[-\rho_2^2/2r_0^2]$ where r_0 is (approximately) the lens radius. To complete the equation for the imaging of the actual scene, we need the expression for $u_2(\rho_2)$ in terms of the scene itself. Applying the extended (H-F) approach², we have

$$u_2(\rho_2) = \frac{-ik}{2\pi z} e^{\frac{ik\rho_2^2}{2z} + ikz} \int d^2\rho_1 e^{-\frac{ik}{z}(\rho_2 \cdot \rho_1) + \frac{ik\rho_1^2}{2z}} u(\rho_1) e^{\psi(\rho_1, 0; \rho_2, z, t)} \quad (3)$$

where z is the longitudinal coordinate.

Equation (3) contains most of the important physics of the problem. This equation differs from the (HF) integral Eq. (1) by the factor $\exp[\psi]$ which contains the effects of the refractive turbulence intervening between

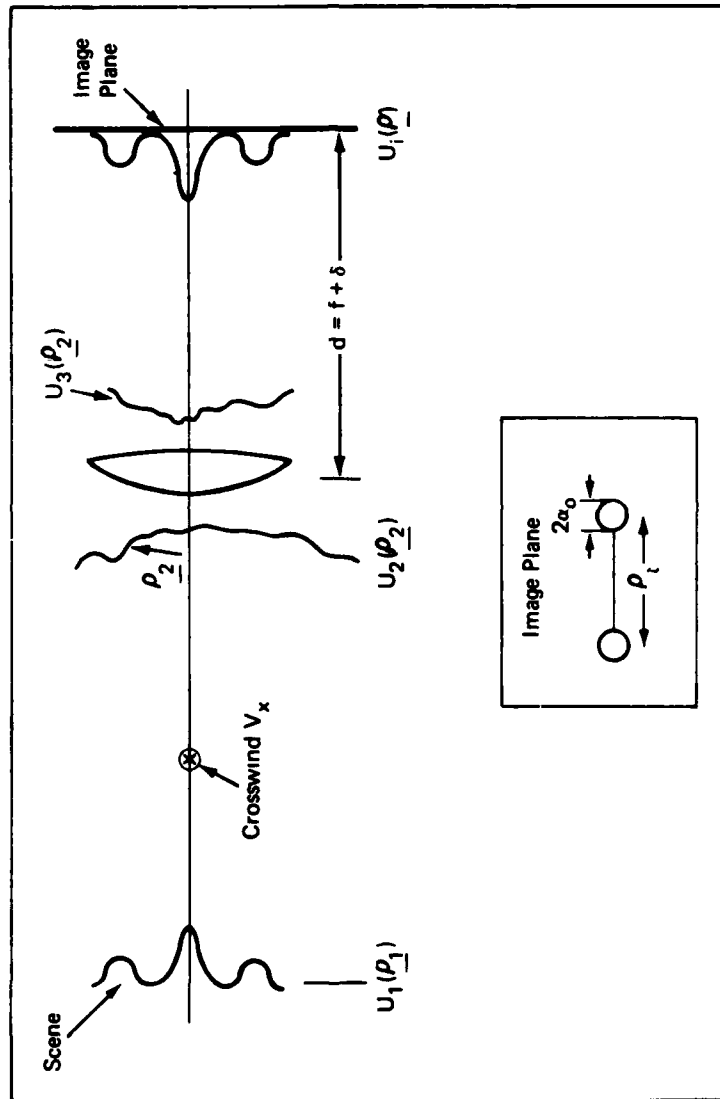


Figure 1. The geometry of the FLIR imaging problem.

source and receiver. The HF approach assumes that you can break up any field distribution e.g., $u_1(\rho_1)$ in Eq. (3) into wavelets originating at each point ρ_1 , propagate them to the receiver and recombine the effects of each wavelet at the receiving plane to obtain the total field. The addition of the factor $\exp[\psi]$ accounts for the effects of refractive turbulence on each wavelet as it propagates from its origin at $(\rho_1, 0)$ to the receiver at (ρ_2, z) . The function $\psi = \chi + i s_1$, where χ is the logamplitude and s_1 is the phase, is the Rytov solution^{3,4} for the logarithmic field of a spherical wave propagating through refractive turbulence.

Inserting Eqs. (2) and (3) into Eq. (1), we have the expression for the image field in the presence of turbulence in the form,

$$u_i(\rho) = \frac{-k^2}{(2\pi)^2 (f + \delta) z} e^{ik(f + \delta + z) + i \left[\frac{k\rho^2}{2(f + \delta)} \right]} \int d^2 \rho_2 \int d^2 \rho_1 e^{i k \rho_1^2 / (2z) - i k(\rho_2 \cdot \rho_1) / z + \psi(\rho_1, 0; \rho_2, z; t)} u(\rho_1) . \quad (4)$$

The image plane of a lens is defined by the relation, $z^{-1} + (f + \delta)^{-1} - f^{-1} = 0$ or where $\delta \approx f(f/z)$. Letting $d = f + \delta$ in the image plane we have

$$u_i(\rho) = \frac{-k^2}{(2\pi)^2 d z} e^{ik(d + z) + i \frac{k\rho^2}{2d}} \int d^2 \rho_2 e^{-i k(\rho_2 \cdot \rho) / d} w(\rho_2) \int d^2 \rho_1 e^{-i k \rho_1^2 / (2z) - i k(\rho_2 \cdot \rho_1) z} e^{\psi(\rho_1, 0; \rho_2, z; t)} u(\rho_1) . \quad (5)$$

Note that in the absence of refractive turbulence ($\psi \rightarrow 0$) and an infinite lens ($W \rightarrow 1$), we obtain

$$u_i(\rho) \propto M^{-1} u(-M^{-1} \rho), \quad (6)$$

the reflected, magnified ($M = d/z$) image that we expect from geometric optics. The effect of refractive turbulence will be to defocus the image and cause it to dance around rapidly in the image plane.

To measure transverse horizontal wind speed, we detect the scintillations with two detectors of radius α_0 separated in the horizontal direction an amount $1/2\rho_t$ on each side of the beam axis. The detected signal takes the form

$$\tilde{I}(\rho_t/2) = (\pi\alpha_0^2)^{-1} \int d^2\rho e^{-(\rho-\rho_t/2)^2/\alpha_0^2} I(\rho), \quad (7)$$

where $I(\rho) = u_i(\rho) u_i^*(\rho)$. By calculating the time-lagged covariance of the two signals $C_I / \langle \tilde{I}_0 \rangle^2$ given by

$$C_I(\rho_t, \tau) = \langle \tilde{I}(\rho_t/2, t) \tilde{I}(-\rho_t/2, t+\tau) \rangle - \langle \tilde{I}_0 \rangle^2, \quad (8)$$

where the angle brackets indicate an ensemble average, $\langle \tilde{I}_0 \rangle$ is the mean irradiance in the weak turbulence limit and statistical stationarity is assumed. We can then compute the slope of this quantity $m = \frac{\partial}{\partial \tau} C_I(\rho_t, \tau)$ which will be proportional to a weighted, path-averaged transverse wind velocity⁵. Substituting Eq. (5) into Eq. (7) and performing the ρ integration using standard tables, we obtain

$$\begin{aligned}
\tilde{I}(\rho_t/2, t) &= \frac{k^4}{(2\pi)^4 d^2 z^2} \int d^2 \rho_2 W(\rho_2) \int d^2 \rho_2' W(\rho_2') e^{i \frac{k \rho_t \cdot (\rho_2 - \rho_2')}{2d}} \\
&\times e^{-\frac{k^2 (\rho_2 - \rho_2')^2 \alpha_0^2}{4d^2}} \int d^2 \rho_1 e^{-\frac{i k \rho_1^2}{2z} - \frac{i k \rho_2 \cdot \rho_1}{z}} u(\rho_1) \\
&\int d^2 \rho_1' e^{\frac{i k \rho_1'^2}{2z} + \frac{i k (\rho_2' \cdot \rho_1')}{z}} u^*(\rho_1') \\
&\times e^{\psi(\rho_1, 0; \rho_2, z; t) + \psi^*(\rho_1', 0; \rho_2', z; t)},
\end{aligned} \tag{9}$$

where $W(\rho_2) = \exp[-\rho_2^2 / 2\tau_0^2]$. Obviously it is extremely cumbersome to write $C_I(\rho_t, \tau)$ directly so we will outline some simplifying arguments first. C_I contains two factors of interest:

$$H(\rho_1, \rho_1', \rho_1'', \rho_1''') = \langle u(\rho_1) u^*(\rho_1') u(\rho_1'') u^*(\rho_1''') \rangle \tag{10}$$

and

$$\begin{aligned}
P &= \langle \exp[\psi(\rho_1, 0; \rho_2, z; t) + \psi^*(\rho_1', 0; \rho_2', z; t) + \psi(\rho_1'', 0; \rho_2'', z; t+\tau) \\
&+ \psi^*(\rho_1''', 0; \rho_2''', z; t+\tau)] \rangle - 1.
\end{aligned} \tag{11}$$

(Subtracting unity in Eq. (11) is valid only in the weak turbulence limit, which we assume in the calculation below.) The quantity H is the fourth moment of the spatial field distribution. If the u 's are representable as joint Gaussian spatially incoherent random fields, then⁶

$$\begin{aligned}
H = H(\rho_1, \rho_1, \rho_1'', \rho_1''') &= \left(\frac{4\pi}{k^2}\right)^2 I(\rho_1) I(\rho_1'') \delta(\rho_1' - \rho_1) \delta(\rho_1''' - \rho_1'') \\
&+ \left(\frac{4\pi}{k^2}\right)^2 I(\rho_1) I(\rho_1'') \delta(\rho_1''' - \rho_1) \delta(\rho_1' - \rho_1'') .
\end{aligned} \tag{12}$$

This assumption simplifies C_I to the form

$$\begin{aligned}
C_I(\rho_t, \tau) &= \left(\frac{k}{\pi z d}\right)^4 \pi^{-2} \\
&\cdot \int d^2 \rho_2 e^{-\rho_2^2 / (2r_o^2)} \\
&\cdot \int d^2 \rho_2' e^{-\rho_2'^2 / (2r_o^2) + \frac{ik\rho_t \cdot (\rho_2 - \rho_2')}{2d} - \frac{k^2(\rho_2 - \rho_2')^2 \alpha_o^2}{4d^2}} \\
&\cdot \int d^2 \rho_2'' e^{-\rho_2''^2 / (2r_o^2)} \\
&\cdot \int d^2 \rho_2''' e^{-\rho_2'''^2 / (2r_o^2) - \frac{ik\rho_t \cdot (\rho_2'' - \rho_2''')}{2d} - \frac{k^2(\rho_2'' - \rho_2''')^2 \alpha_o^2}{4d^2}} \\
&\cdot \int d^2 \rho_1 I(\rho_1) \\
&\cdot \int d^2 \rho_1'' I(\rho_1'') \left[e^{-\frac{ik\rho_1 \cdot (\rho_2 - \rho_2')}{z} - \frac{ik\rho_1'' \cdot (\rho_2'' - \rho_2''')}{z}} P_1 \right. \\
&\quad \left. + e^{-\frac{ik\rho_1 \cdot (\rho_2 - \rho_2''')}{z} - \frac{ik\rho_1'' \cdot (\rho_2'' - \rho_2')}{z}} P_2 \right] \tag{13}
\end{aligned}$$

the next problem is to evaluate the P's. If we make the reasonable assumption that the bulk of the propagation effects arise from the influence of phase fluctuations, Lee et al.⁷ have shown that

$$\begin{aligned}
P + 1 = \exp\{ & -\frac{1}{2} [D(\rho_1 - \rho_1', \rho_2 - \rho_2', 0) - D(\rho_1 - \rho_1'', \rho_2 - \rho_2'', \tau) \\
& + D(\rho_1 - \rho_1''', \rho_2 - \rho_2''', \tau) - D(\rho_1' - \rho_1''', \rho_2' - \rho_2''', \tau) \\
& + D(\rho_1' - \rho_1'', \rho_2' - \rho_2'', \tau) + D(\rho_1'' - \rho_1''', \rho_2'' - \rho_2''', 0)] \} \quad (14)
\end{aligned}$$

where D is the two point source, two receiver "wave" (or approximately "phase") structure function defined by $D(\underline{x}, \underline{y}, \tau) = \langle [\psi(\underline{x}', \underline{y}', \tau') + \psi^*(\underline{x}' + \underline{x}, \underline{y}' + \underline{y}, \tau' + \tau)]^2 \rangle$ and equal to⁸

$$D(\underline{x}, \underline{y}, \tau) = 4\pi k^2 z \int_0^1 dt \int d^2 \underline{k} \Phi_n(\underline{k}, t) \left[1 - e^{i \underline{k} \cdot [\underline{x}(1-t) + \underline{y}t - \underline{v}(t)\tau]} \right], \quad (15)$$

where Φ_n is the refractive-index power spectral density, t is the normalized path position, z is the total path length and \underline{v} is the wind velocity. To further simplify the calculation, we make the weak turbulence assumption, valid for IR, $\exp[A] \sim 1 + A$. Further, we drop terms that are time independent and therefore do not affect the slope at zero time lag. Under these approximations, P_1 and P_2 could be obtained by letting $\rho_1 = \rho_1'$, $\rho_1''' = \rho_1'' = \rho_1''$ respectively, i.e.,

$$\begin{aligned}
P_1 = \frac{1}{2} [& D(\rho_1 - \rho_1'', \rho_2 - \rho_2'', \tau) - D(\rho_1 - \rho_1''', \rho_2 - \rho_2''', \tau) \\
& + D(\rho_1 - \rho_1'', \rho_2' - \rho_2''', \tau) - D(\rho_1 - \rho_1'', \rho_2' - \rho_2'', \tau)]
\end{aligned}$$

and

$$\begin{aligned}
P_2 = \frac{1}{2} [& D(\rho_1 - \rho_1'', \rho_2 - \rho_2'', \tau) - D(0, \rho_2 - \rho_2''', \tau) \\
& + D(\rho_1'' - \rho_1', \rho_2' - \rho_2''', \tau) - D(0, \rho_2' - \rho_2'', \tau)]. \quad (16)
\end{aligned}$$

To simplify Eq. (13), we insert Eq. (15) and Eq. (16) and make the changes of variables $\xi = \rho_1 - \rho_1''$, $2\eta = \rho_1 + \rho_1''$; $\xi_1 = \rho_2 - \rho_2'$, $2\eta_1 = \rho_2 + \rho_2'$; $\xi_2 = \rho_2'' - \rho_2'''$, $2\eta_2 = \rho_2'' + \rho_2'''$ and integrate over η_1 and η_2 to obtain

$$C_I(\rho_t, \tau) = 4k^2 z \left(\frac{kr_o}{zd} \right)^4 \int_0^1 dt \int d^2 K e^{-iK \cdot v \tau} \phi_n(K, t) \int d^2 \xi \int d^2 \eta$$

$$I(\eta + \frac{1}{2} \xi) I(\eta - \frac{1}{2} \xi) \int d^2 \xi_1 \int d^2 \xi_2 e^{\frac{ik}{2d} \rho_t \cdot (\xi_1 - \xi_2) - \frac{k^2 \alpha_o^2}{4d^2} (\xi_1^2 + \xi_2^2)}$$

$$e^{-\frac{ik}{z} \eta \cdot (\xi_1 + \xi_2)}$$

$$\left\{ e^{-K^2 t^2 r_o^2 / 2 - \frac{ik}{(2z)} \xi \cdot (\xi_1 - \xi_2) + iK \cdot \xi (1-t)} \left[\cos \left[K \cdot \left(\frac{\xi_1 + \xi_2}{2} \right) t \right] - \cos \left[K \cdot \left(\frac{\xi_1 - \xi_2}{2} \right) t \right] \right] \right.$$

$$\left. + e^{-(Kt - k\xi/z)^2 r_o^2 / 2} \left[\cos \left[K \cdot \left(\frac{\xi_1 + \xi_2}{2} \right) t \right] - e^{iK \cdot \xi (1-t)} \cos \left[K \cdot \left(\frac{\xi_1 - \xi_2}{2} \right) t \right] \right] \right\} \quad (17)$$

valid for $k\alpha_o/d \gg r_o^{-1}$. (For our problem $\alpha_o/d \sim 10^{-3}$, $k \sim 2\pi \times 10^5 \text{ m}^{-1}$ and $r_o = 7 \times 10^{-2} \text{ m}$ so $k\alpha_o/d \sim 630 \text{ m}^{-1}$ and $r_o^{-1} \sim 14 \text{ m}^{-1}$.) To continue, we let $2y = \xi_1 + \xi_2$, $x = \xi_1 - \xi_2$ and perform the x , y integrations, resulting in the expression

$$C_I(\rho_s, \tau) = 32\pi k^2 z \left(\frac{r_o}{2\alpha_o} \right)^4 \int_0^1 dt \int d^2 K e^{-iK \cdot v \tau} \phi_n(K, t)$$

$$\int d^2 \xi \int d^2 \eta I(\eta + \frac{1}{2} \xi) I(\eta - \frac{1}{2} \xi) \left\{ e^{-K^2 t^2 r_o^2 / 2 + iK \cdot \xi (1-t)} \right.$$

$$\times [F(\xi - \rho_s, 2\eta \pm Ktz/k) - F(2\eta, \xi - \rho_s \pm Ktz/k)]$$

$$\left. + e^{-(Kt - k\xi/z)^2 r_o^2 / 2} [F(\rho_s, 2\eta \pm Ktz/k) - e^{iK \cdot \xi (1-t)} F(2\eta, \rho_s \pm Ktz/k)] \right\} \quad (18)$$

where $\rho_s = \rho_t z/d$, $\alpha_s = \alpha_o z/d$ and

$$F(\tilde{x}, \tilde{y} \pm a) = e^{-\tilde{x}^2/(2\alpha_s^2)} \left[e^{-(\tilde{y}-a)^2/(2\alpha_s^2)} + e^{-(\tilde{y}+a)^2/(2\alpha_s^2)} \right]. \quad (19)$$

Now we must insert some model of our FLIR target. A useful model and one directly applicable to our experiments is the horizon where

$$I(\tilde{r}) = \begin{cases} 0 & r_y \geq 0 \text{ all } r_x \\ 1 & r_y < 0 \text{ all } r_x. \end{cases} \quad (20)$$

Note for this form of I that

$$I(\eta_y + \frac{1}{2} \xi_y) I(\eta_y - \frac{1}{2} \xi_y) = I(\eta_y + \frac{1}{2} |\xi_y|).$$

Inserting this into Eq. (18) we can start the tedious but straightforward process of integrating over ξ and η' . Performing the calculation, for weak refractive turbulence and for $z/(k r_o \alpha_s) \ll 1$, we obtain

$$\frac{C_I(\rho_s, \tau)}{\langle I_o \rangle^2} = 16\pi k^2 z \int_0^1 dt \int d^2 \tilde{K} e^{iK \cdot [\rho_s(1-t) - \tilde{v}(t)\tau]} \Phi_n(\tilde{K}, t) e^{-K^2 t^2 r_o^2/2 - K^2(1-t)^2 \alpha_s^2/2} \sin^2 \left[\frac{K^2 z t(1-t)}{2k} \right] \left[1 - \text{erf}^2 \left(\frac{iK_y(1-t)\alpha_s}{2} \right) \right] \quad (21)$$

where we have normalized C_I by $\langle I_o \rangle^2$. (Note the last two terms in Eq. (18) contribute nothing to the slope at zero lag for the particular target that we have assumed.)

From Eq. (21) we compute the slope at zero lag m contributed by the x-directed or horizontal wind component ($\hat{x} \parallel \rho_s$),

$$m = \int_0^1 dt C_n^2(t) v_x(t) W(t) , \quad (22)$$

where the wind- C_n^2 weighting function W is given by

$$W(t) = 0.528\pi k^2 z \int_{-\infty}^{\infty} dk_x K_x \sin [K_x \rho_s (1-t)] \int_{-\infty}^{\infty} dk_y K^{-11/3} e^{-K^2 t^2 r_o^2 / 2 - K^2 (1-t)^2 \alpha_s^2 / 2} \sin^2 \left[\frac{K^2 z t(1-t)}{2k} \right] \left[1 - \text{erf}^2 \left(\frac{1 K_y (1-t) \alpha_s}{2} \right) \right] . \quad (23)$$

(Note the y-directed, vertical wind component will not contribute to m .) We have inserted the Kolmogorov form^{3,4} of the refractive index spectrum in Eq. (23), that is,

$$\Phi_n(K, t) = 0.033 C_n^2(t) K^{-11/3} \quad (24)$$

valid if $L_o^{-1} \ll K \ll \ell_o^{-1}$ where L_o and ℓ_o are respectively, the outer scale and microscale of the refractive index fluctuations.

Although Eqs. (21) and (23) were derived for phase-variation-induced image fluctuations and their ultimate contribution to irradiance fluctuations, the form of these equations suggest a convenient analog. When comparing Eq. (21) with Eq. (9) of Clifford et al.,⁹ it is apparent that a completely analogous calculation to the FLIR problem with a horizon target is wind sensing using two, half-moon, spatially incoherent sources with their flat edges oriented in the x direction and displaced an amount ρ_s parallel to their edges. In this analog, these sources, that are located at the FLIR target plane, must be coded and observed with two co-located receivers at the aperture of the FLIR. The equivalent sources and receivers must have the amplitude weighting function

$$\exp[-(x^2+y^2)/\alpha_s^2] \text{ for } y \leq 0 \text{ and } \exp[-(x^2+y^2)/r_o^2] ,$$

respectively. We have previously analyzed this problem⁹ and the applicable wind weighting functions peaked closer to the receiver (FLIR), than toward the transmitter (target) by an amount depending on the ratio of the source and receiver radii. As will be shown in the next section, this is qualitatively observed in our FLIR experiments. A computer analysis of Eq. (23) will be undertaken to give precise results for our experimental conditions.

A rough idea of the shape of the wind weighting function and its dependence on (r_o/α_s) can be seen as follows: If we note for $r_o < \alpha_s$ that $Kt \leq r_o^{-1}$ in the integrand of Eq. (23) then, in the $\sin^2\theta$ term, if we ignore the end points where $W(t) = 0$ and use $\sin \bar{t} \sim \frac{1}{2}$, $\theta = z/(kr_o^2) < 1$ and $\sin^2\theta \sim \theta^2$ is a reasonable approximation. With this assumption and a change of variables to $K' = K(1-t)$, we obtain

$$W(t) \propto \frac{t^2}{(1-t)^{4/3}} \int_{-\infty}^{\infty} dK_x' K_x' \sin(K_x' \rho_s) \int_{-\infty}^{\infty} dK_y' (K_y'^2 + K_x'^2)^{1/6} \exp\left[\frac{-K'^2 t^2 r_o^2}{2(1-t)^2}\right] e^{-K'^2 \alpha_s^2/2} [1 - \text{erf}^2(iK_y' \alpha_s/2)] . \quad (25)$$

We note that, if $\rho_s \sim \alpha_s$, $K' \sim \sqrt{2}/\alpha_s$ in the important region of integration in both K_y' and K_x' , then we obtain as a rough approximation

$$W(t) \propto \frac{t^2}{(1-t)^{4/3}} e^{-\frac{t^2(r_o/\alpha_s)^2}{(1-t)^2}} . \quad (26)$$

A plot of this function is shown in Fig. 2 for $r_o/\alpha_s = 1$ (dotted line) and $r_o/\alpha_s = 0.5$ (solid line). The plot compares favorably with the experimental results in Section 3. In general, the weighting function Eq. (26) and the

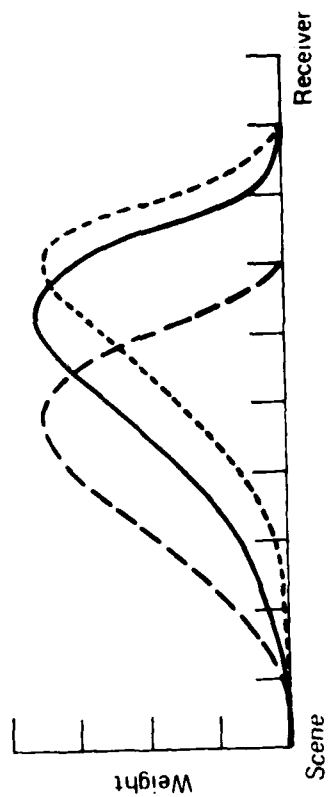


Figure 2. Analytically derived approximate wind weighting functions for $r_o/a_s = 1/2$ (dashed line), $r_o/a_s = 3/8$ (dotted line), and $r_o/a_s = 1$ (solid line).

approximations above indicate that the peak of the weighting function is at $t_m \approx (1 + r_o/\alpha_s)^{-1}$ and the most important scale size for producing fluctuations is $\ell \sim \sqrt{2\pi} (r_o^{-1} + \alpha_s^{-1})^{-1}$.

3. EXPERIMENTAL MEASUREMENTS

3.1 Wind Measurements at Visible Wavelengths

All of the field measurements for this study were made at Table Mountain, a mesa having a flat area of about 1.5 by 3 km, and located 12 km north of Boulder, Colorado. Figure 3 shows a view looking down the 500 m test range used for the experiments. The two trailers and the surface of the mesa surrounding them comprised the scenes observed.

For the visible experiments, a Schmidt-Cassegrain telescope of 22.3 cm diameter was focused to form an image on a dual photodiode by eyepiece projection, as in Fig. 4. The angular fields of view were determined by the size of the image on the photodiode surfaces. The electrical signals from the photodiodes were then processed as follows: The normalized covariance versus time delay was observed in real time by a correlator. Two particular properties of the covariance, its slope at zero time delay and an analysis based upon a sampling of the function at 14 time delays¹⁰ were computed. Averaged values of these quantities, together with information from a propeller anemometer array and an optical C_n^2 meter, were logged by a mini-computer which also computed the weighting functions for the optical wind measurement.

Typical covariance functions are shown in Fig. 5. According to the theory, the propagation characteristics for the optical geometry used should be very similar to that which would exist if the system were replaced



Figure 1. A large, dark, textured object, possibly a piece of wood or a large rock, standing vertically. The object has a small, light-colored rectangular label attached to its side. The background is bright and shows some horizontal lines, possibly a fence or a wall.

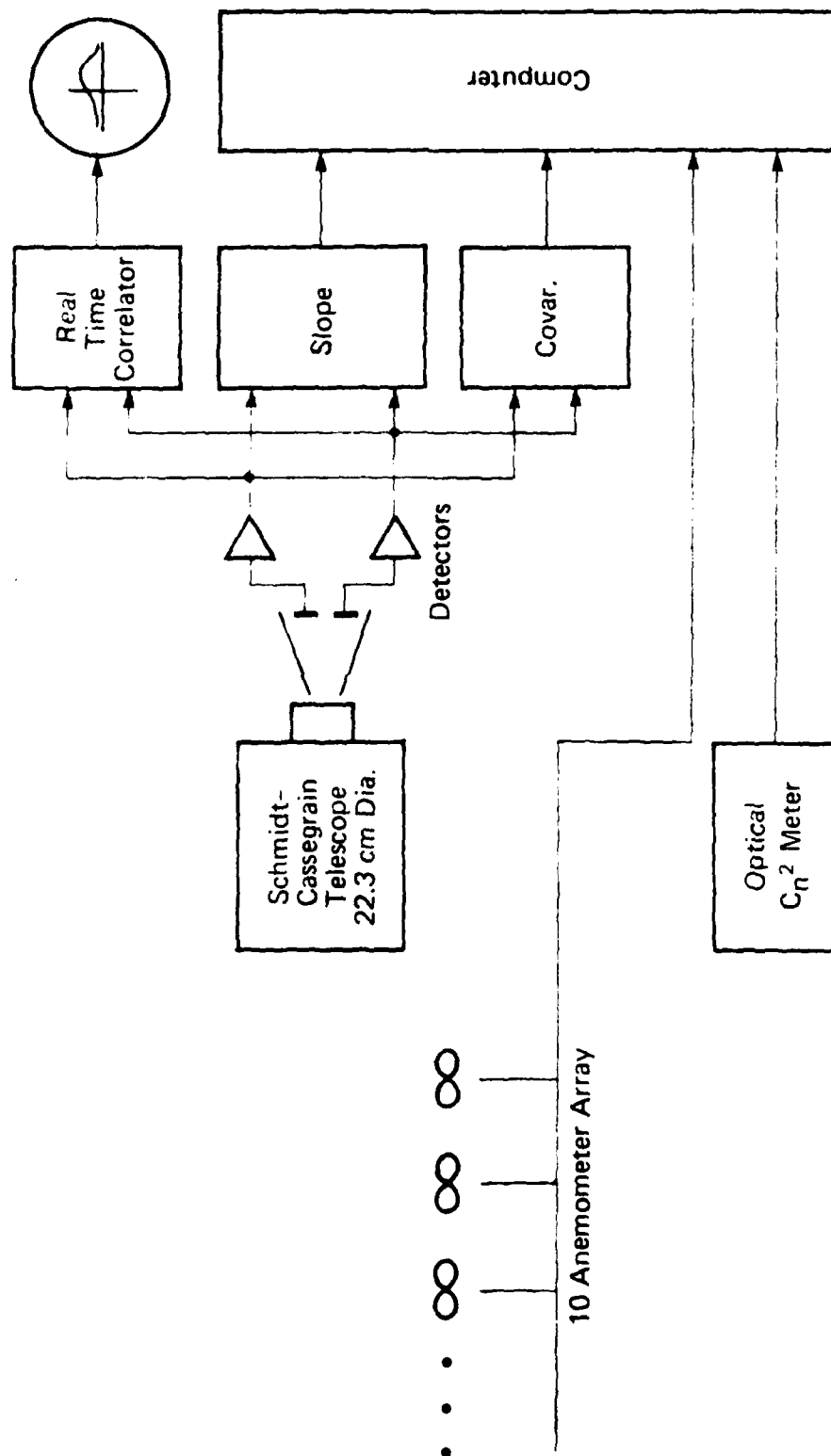


Figure 4. Block diagram of the experiment at visual wavelengths.

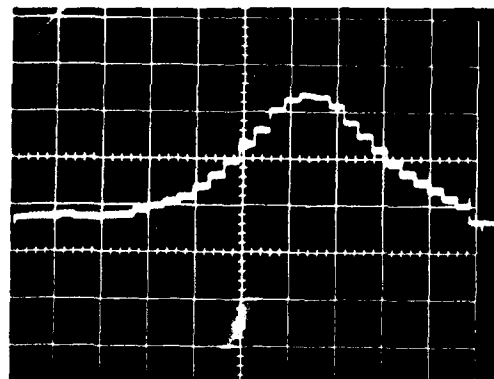
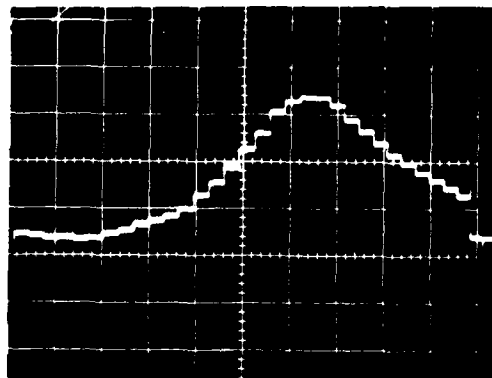
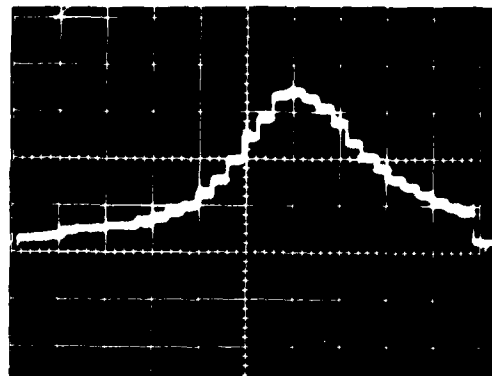


Figure 5. Covariance functions at visual wavelengths. The time scale is 10 ns per delay bit.

by a detecting aperture the size of the receiver (22.3 cm) and two radiating, half-moon, apertures the diameter of the projected area of the detectors on the scene (40 cm). With this geometry one would expect from the theory a peak response to winds about $t \sim 1.22 r_o / \alpha_s = 0.68$ of the way from the scene, and maximum sensitivity to irregularities of spatial wavelength about $(2\pi K^{-1}) \sim 2\pi \alpha_s / (3\sqrt{2}) = 30$ cm. Since the average crosswind was measured by anemometers during the covariance function measurement, the spatial wavelength can be estimated. It turns out to be 30 cm, in agreement with the prediction. The weighting function was also measured (Fig. 6) and its peak response was as predicted.

In the experiment, we looked at the horizontal edge of the window of the trailer which was dark against the light outside of the trailer. The horizontal edge also assured that both detectors saw the same scene spatial spectrum. The theory of course shows that any measure of wind by this technique is a function of the scene spatial spectrum, and since the detectors are observing relatively small portions of the scene, in general wide variations in the spectrum may be expected. In practice this means that wind information can only be obtained from certain portions of the scene. At first it was thought that by averaging the information from many pairs of detectors observing the scene, the signal-to-noise of the wind measurement could be improved by something like the square root of the number of pairs of detectors. Experience has shown that this would not be the case. In fact, one pair of detectors at a particularly favorable location in the scene will very likely have better signal-to-noise than the average of many pairs. With many pairs of detectors available, however, one would have the advantage of being able to choose, by criteria such as scintillation level and correlation, the detector pairs having the best signal-to-noise for wind measurement.

Figure 7 shows comparisons of wind measurements obtained by the slope and covariance techniques with the average of 10 propeller anemometers along the light path for a sunny period of 3 hours in the afternoon of October 3, 1979. An optical measurement of C_n^2 is also shown. The optical measurements

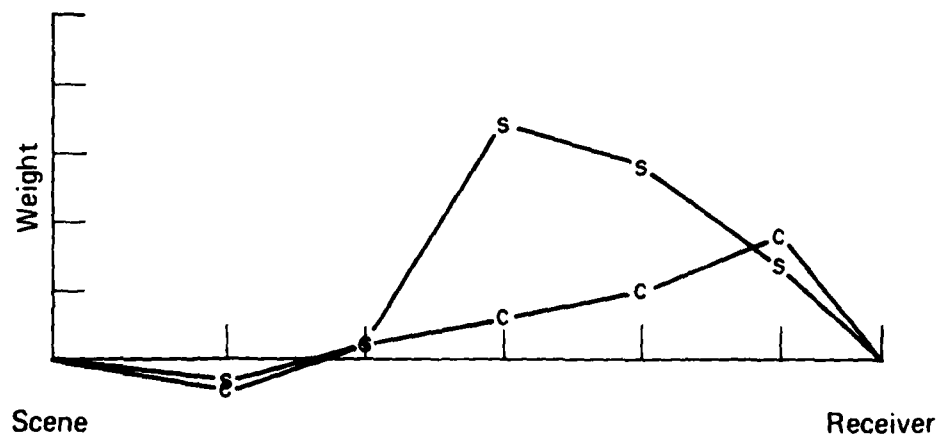
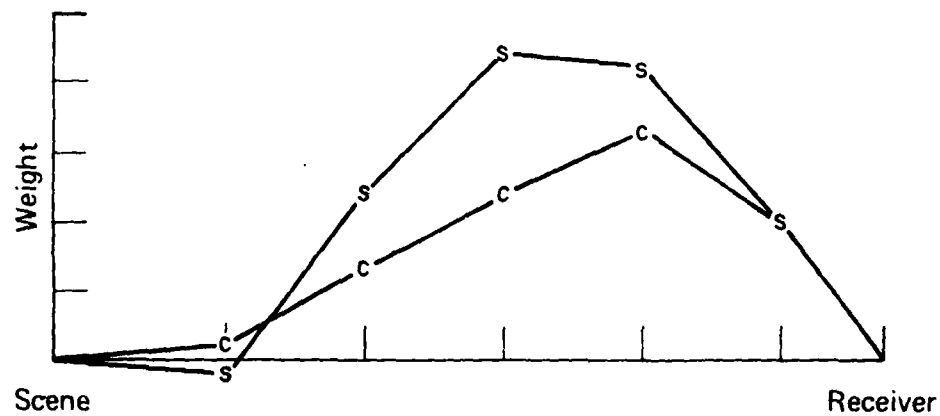


Figure 6. Experimental weighting functions for wind measurement for slope (S) and covariance (C) methods of analyzing the data. The upper graph is for a projected aperture size of 20 cm at the scene; the lower graph is for 40 cm.

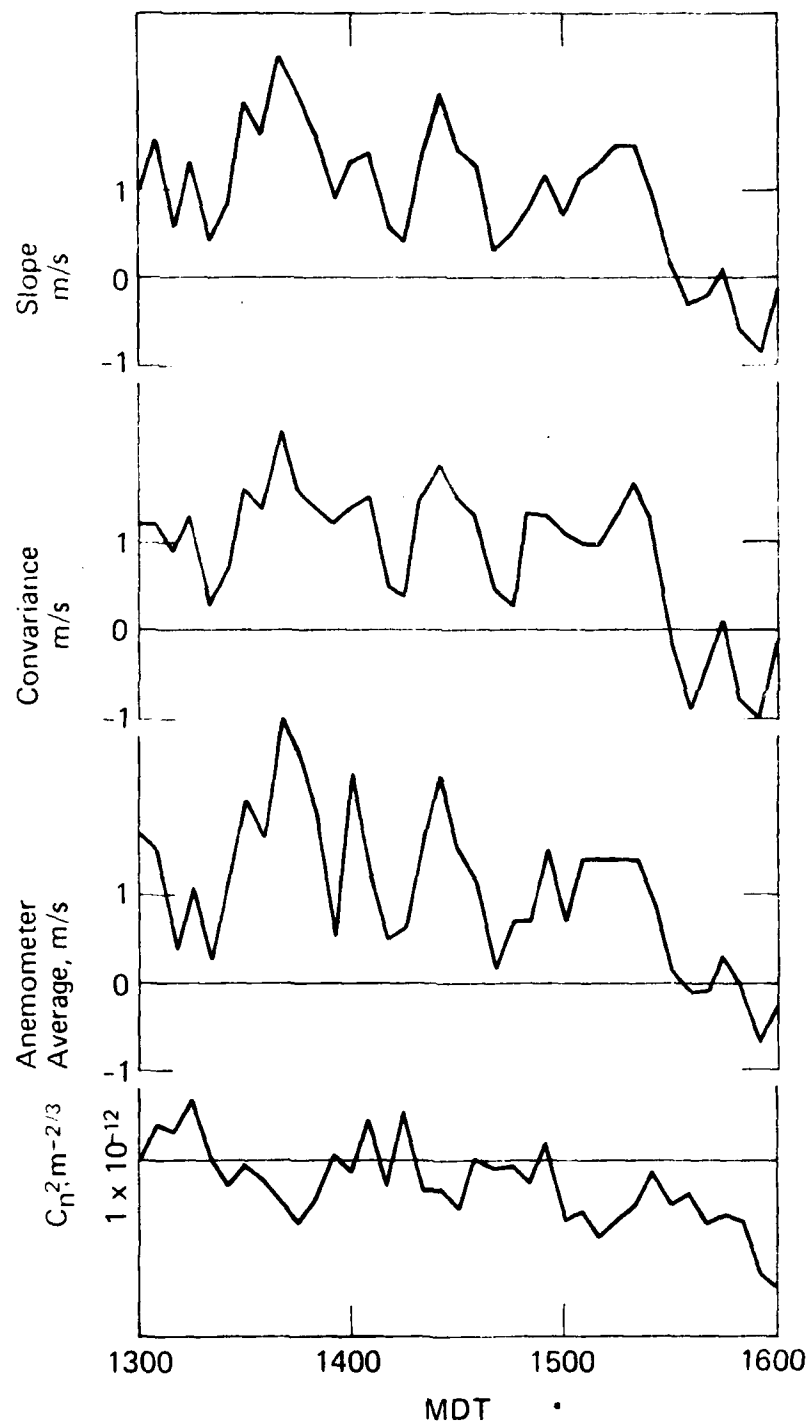


Figure 7. Optically derived wind speeds compared with the average of 10 propeller anemometers along the optical path. The scintillation level during the experiment is also shown.

correlate well with the anemometer averages; however, the conditions of high C_n^2 and a carefully selected target were ideal and it is clear that the system could not be depended on to operate in more adverse conditions.

3.2 Wind Measurements from FLIR Thermal Sight Signals

Personnel from the Atmospheric Sciences Laboratory, White Sands Missile Range, New Mexico, provided an AN/VSG Thermal Sight of the tank-mounted type, set up the system on Table Mountain and explained its operation. They also provided a high-speed 14-channel instrumentation tape recorder and worked with NOAA personnel to record the data which is analyzed and presented in this section.

References 11 and 12 describe the thermal sight. It is described as an integrated day/night fire control periscope for the M60A1(PI) main battle tank. It combines a daylight optical viewing system, a self-contained ballistic reticle projector, and a high-resolution passive thermal imaging system that provides both surveillance and fire control capability to commander and gunner during day and night battlefield conditions. Some of the data pertinent to our study are listed in table 1. The image is formed by scanning a vertical array of 120 IR detectors horizontally across the image plane with a scanning mirror, then shifting vertically by one-half the detector spacing for an interlaced return trace, at the rate of 42 of these cycles per second. The electrical signals from these detectors drive LEDs which are scanned with the same mechanical assembly to form a visual image. The video signals from all 120 detectors, as well as a sync pulse at 84 Hz, are readily available. The test setup for recording video data from the thermal sight is shown in Fig. 8. Three adjacent detector scans, the sync pulse, voice annotation, and 9 propeller anemometers were tape recorded. A separate chart recorder continuously recorded C_n^2 levels from an optical meter. The video bandwidth of the

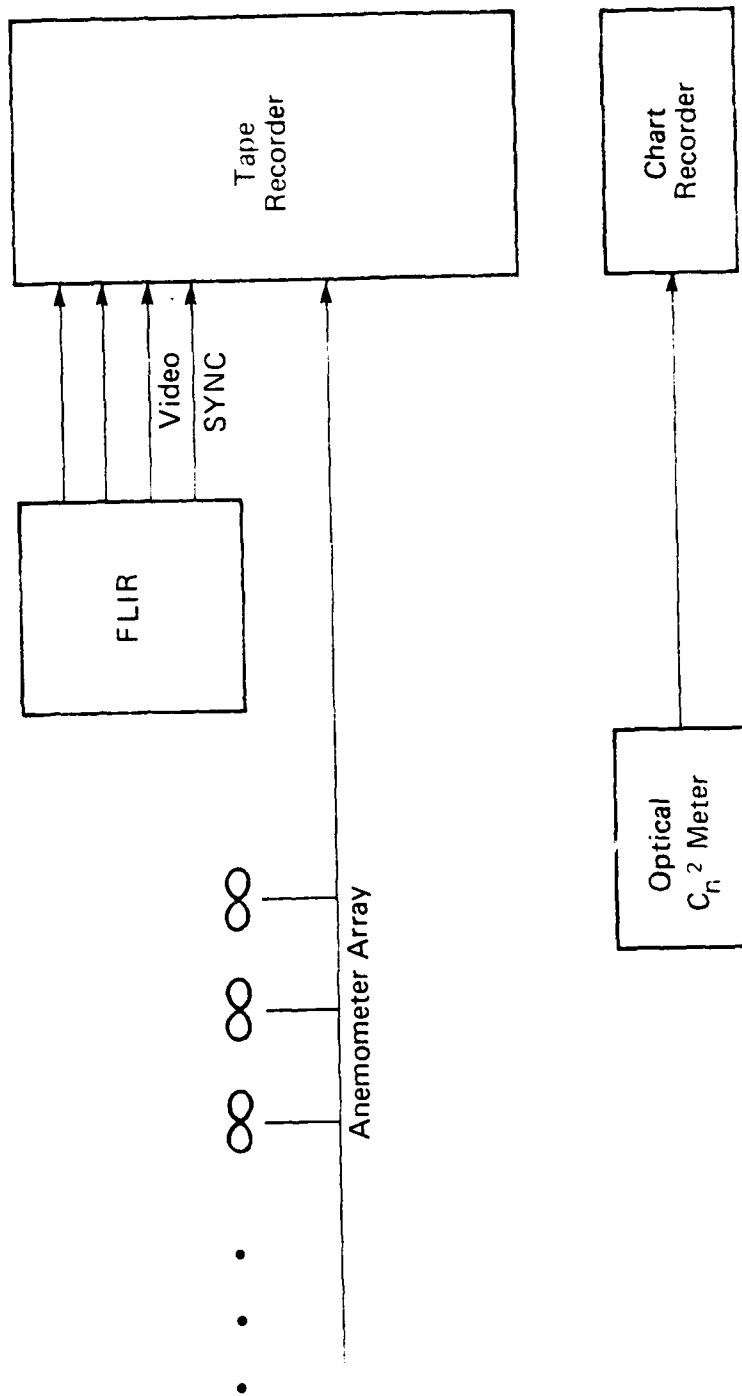


Figure 8. Block diagram of FLIR thermal sight experiment.

TABLE 1. THERMAL CHANNEL PARAMETERS FOR NARROW FIELD OF VIEW

Field of view (degrees)	2.58 x 5
Frame rate	42 Hz
Interlace ratio	2:1
Scan efficiency	0.70
Germanium primary lens	
Diameter	15.2 cm
Effective focal length	27.1 cm
Detector	
Type	Mercury cadmium telluride
Number of elements	120
Spectral wavelength	7.6 to 11.75 micrometers

FLIR is 70 kHz, but it was reduced to 23 kHz in the recording process. This bandwidth resulted in a horizontal angular resolution of about 60 μ rad.

As in the experiment at visible wavelengths, we wish to examine the changes in brightness at a particular location in the image plane, and correlate these changes with those at another location, horizontally displayed from the first. Ideally, one would like to do this for all possible pairs of horizontally displaced points. Two approaches were considered for this analysis. One was to digitize a small portion of the video record at a very high rate (>50 kHz). Due to the low frequencies present in the signal, however, this sample would have had to be about 5 to 10 seconds long. Another way would be to synchronize the beginning of the digitizing with the video sync pulse, and then digitize a portion of every other trace, starting at the same location on each trace. In fact, portions of the video tape recordings were digitized in the latter

way, at an 8 kHz rate. It soon became clear, however, that this rate would not really be adequate, and that in addition, it would not be as advantageous to average the correlation functions of many pairs of points as we first thought it would be.

We had planned to use another method to preview the tape recorded information, but it turned out to be the best method for the entire analysis. Only one pair of points could be analyzed at once, but there was no bandwidth limitation, the traces could be monitored in real time on an oscilloscope, there was a high degree of flexibility, and most important, nearly instantaneous turnaround time. A block diagram of the analysis technique is shown in Fig. 9. The sync signal and the video signal from one of the detectors enters the sample and hold circuit enclosed by the dotted line. This specially designed circuit operates as shown in Fig. 10. A time delay ℓ from the end of the sync pulse is adjusted to sample at the desired location on the trace. At this time the signal amplitude is sampled and held until the interlace sweep is completed and the original trace is beginning again. The signal is again sampled at the same location on the trace and held. Disregarding jitter and other system noise, the fluctuations in the level of this sampled waveform represent changes in brightness at a fixed location in the image plane. A second sampled waveform is generated by sampling and holding the signal amplitude of the video trace at a time delayed by $\Delta\ell$ from the sample times of the first trace. The normalized covariance of these signals can then be computed in the same way that it was done at visible wavelengths for the continuous signals obtained from fixed detectors, horizontally separated in the focal plane.

Since the sampling rate is 42 per second, signal fluctuations above 21 Hz cannot be observed. In fact because of noise the frequency limitation is even lower; this limits the maximum wind speed that can be measured, and the data shows this effect.

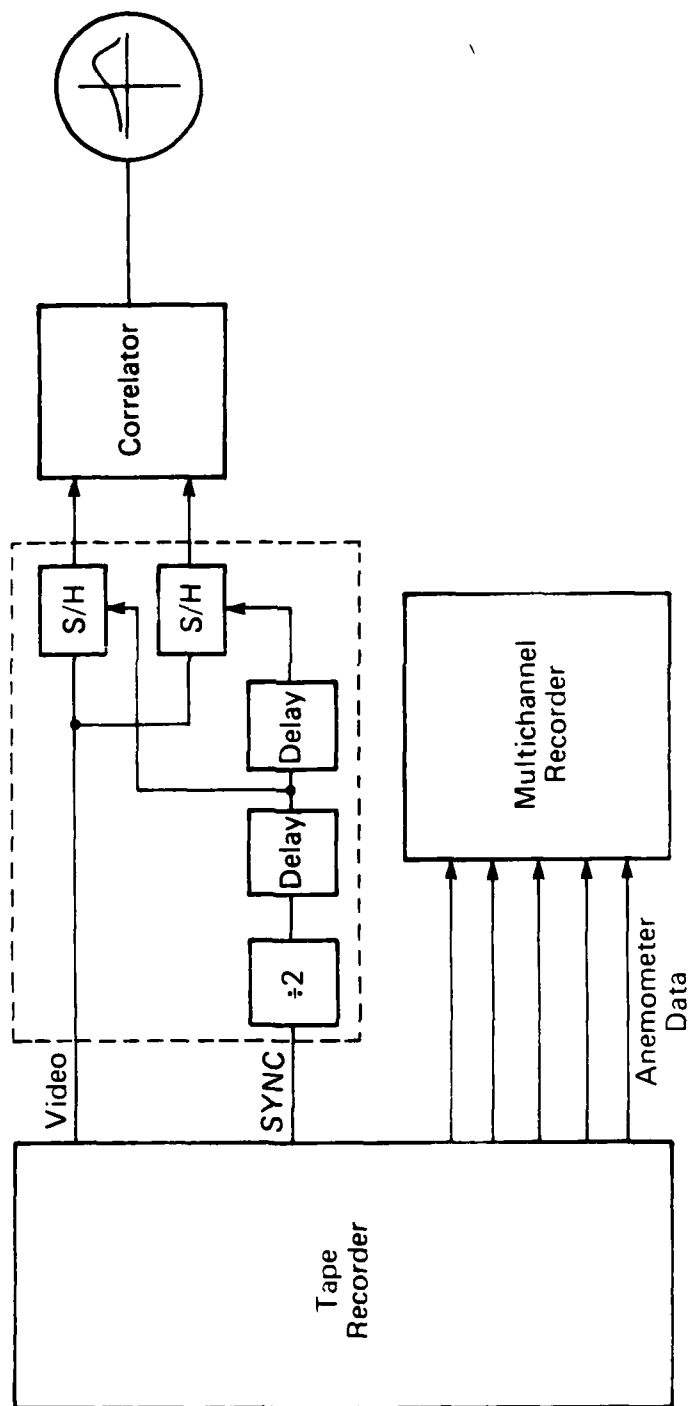


Figure 9. FLIR analysis technique.

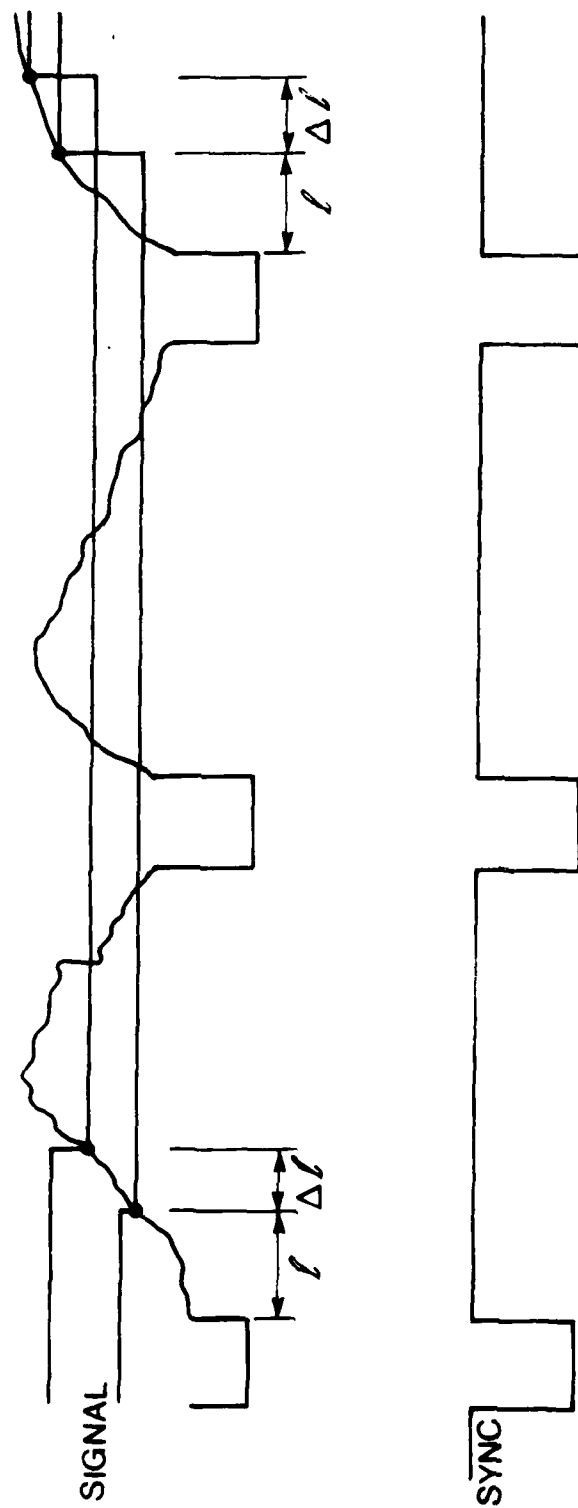


Figure 10. Sample and hold system.

About 75 minutes of FLIR data were recorded on 10 rolls of magnetic tape on February 7, 8, 9, 12, 13, 14, 15, and 21, 1979. We examined all of the tapes but chose to analyze intensively tapes 7, 8, 9, and 10 taken on February 14 and 21. Covariance functions for 2 sample points taken 100 μ s apart from data on tapes 7, 8 and 9 are shown in Figs. 11 through 13. Full scale plus and minus on the ordinate represents a normalized covariance of +1 and -1 respectively. On the abscissa, the time scale is 30 ms per bit or .96 s full scale for all figures except Fig. 16, which is 60 ms per bit or 1.92 s full scale. The time delay Δt between the samples from which the covariance is computed is 100 μ s, except for Figs. 14, 15, and 16, where it is 25, 50, and 200 μ s, respectively. The covariance estimate is made from 20 s of data in each case. The time sequence for the covariance functions progresses from upper left to lower right.

Generally, a covariance function with a time-delayed peak corresponding to the existing crosswind was observed. The series in Fig. 12 is representative. In this case, the direction of the crosswind changed during the run, shifting the peak from positive to negative delays.

Knowing the average wind speed from anemometer readings (0.6 m/s) and obtaining from Fig. 12 the average time delay to the peak of the covariance function (0.2s), we can estimate the separation in space of the light beams as 0.6 m/s x 0.2 s = 0.12 m. If the sampled points on the trace are separated by 100 μ s, the angular divergence α of the rays from these points to the scene is

$$\alpha = \frac{100 \mu\text{s}}{10 \text{ ms}} \times \frac{5^\circ}{57.3^\circ/\text{rad}} = 8.73 \times 10^{-4} \text{ rad.}$$

Roughly then, the wind weighting function should peak up at a distance (1-t) from the receiver, or

$$(1-t) = \frac{0.12}{8.72 \times 10^{-4}} = 137 \text{ m,}$$

which is very close to the prediction of Eq. (26), using a 15 cm receiving aperture and detectors whose effective projection size at 500 m are 0.5 m.

Using this calibration, we plot in Fig. 18 a comparison of the propeller anemometer average versus the optical measurement of wind. While the data from tape 8 compares quite well, the optical measurement is too low for the data on tapes 7 and 9. This result is expected since the 42 Hz sampling rate would limit the frequency response so that for this geometry, 2 m/s winds would be about the maximum speed that could be measured.

Higher wind speeds could in principle be measured by shortening the sample interval time Δt . Both the resolution of the system and the atmosphere limit the minimum time, however. Figures 14, 15, 11, and 16 show the same data on tape 8 analyzed using sampling delays of 25, 50, 100 and 200 μ s. The 25 μ s data show some time delayed covariance, but mostly peak up around zero time delay. This is a result of insufficient video bandwidth. While the FLIR system had sufficient bandwidth, the recording system had less than half of the frequency response required to record this signal accurately. There is nearly enough bandwidth available for the measurements made at 50 μ s intervals (Fig. 15). One can see that the peak delay is about half of that at 100 μ s (Fig. 11) although there is some tendency to peak around zero delay. From the theory one would expect that some peaking symmetric with zero time delay could occur due to back and forth tilts of the optical wave front near the receiving aperture. At 200 μ s (Fig. 16, note time scale change), the peak delays are twice as long, as one would expect, but also there is evidence of less covariance at the wider spacing.

An example of the sensitivity of the system to a particular portion of the scene is shown by the bottom graph in Fig. 12. It shows the covariance function obtained from signals obtained during the return trace. The field of view of this trace is vertically displaced only 0.2 m/s at the scene from the one used to obtain all the rest of the data but no useful wind information could be obtained from it.

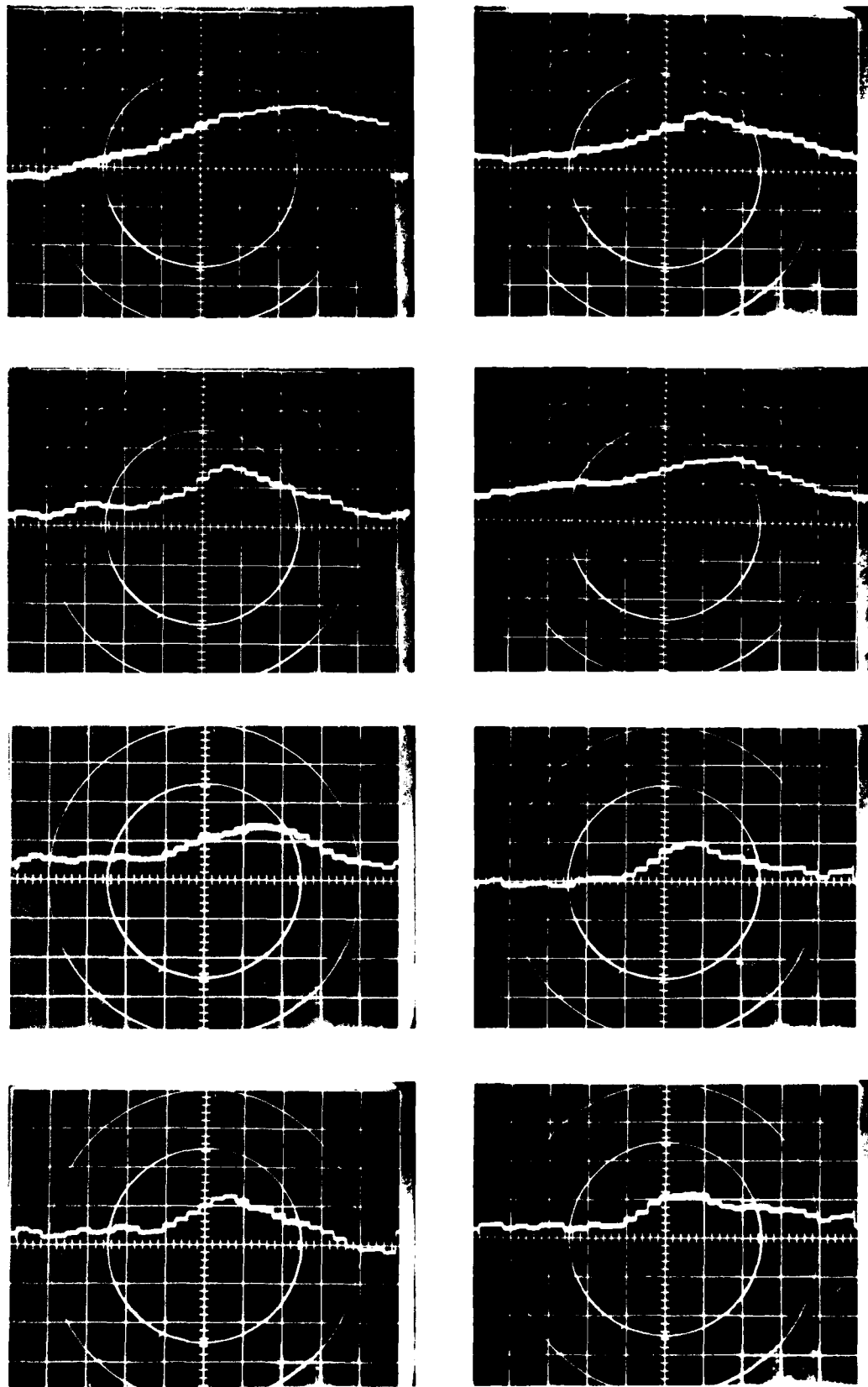


Figure 11. Covariance functions from FLIR data starting 1049 February 14, 1979, the view just grazes the top of Table Mountain. C_u^2 is 1 to 2×10^{-13} , with the sun in and out of clouds. The delay is 40 ms per bit and the range is 1000 ft.

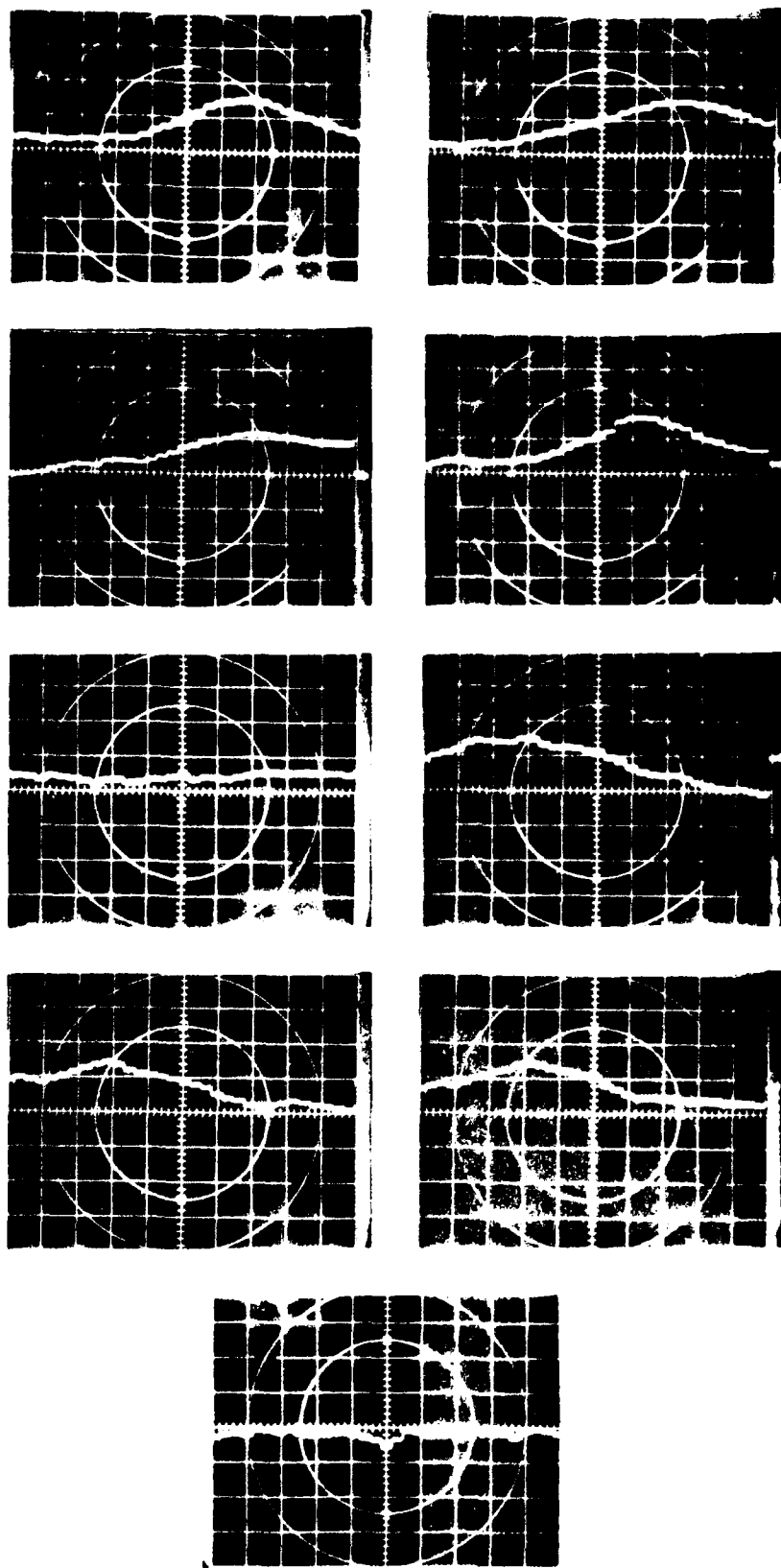


Figure 12. Covariance functions from FLIR data starting 1108 February 14, 1979.

The view is just grazing the top of Table Mountain. C_p^2 is $3 \text{ to } 6 \times 10^{-13}$.

The delay is 30 ms per bit and the sample interval is 100 μ s. The function shown at bottom center is from the reverse trace at a slightly different location in the image plane.

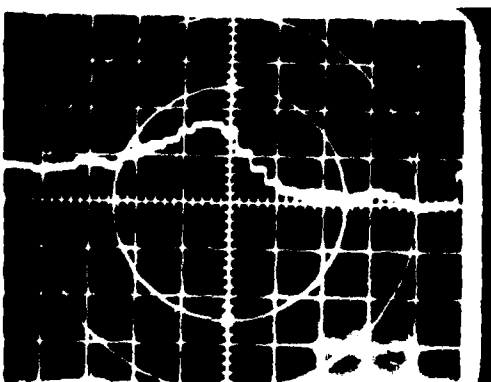
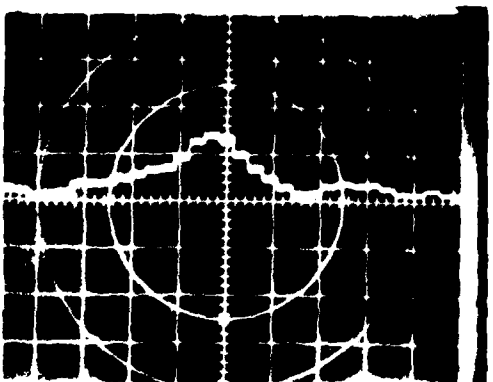
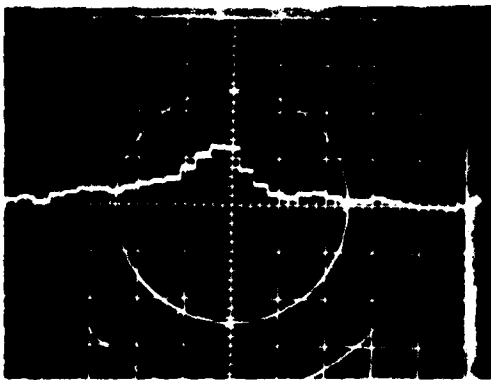
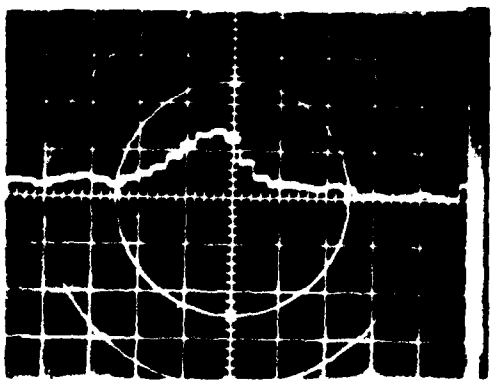
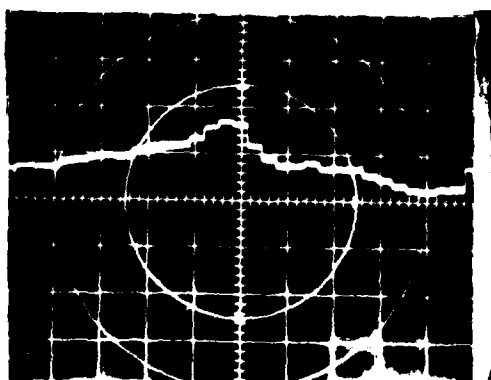
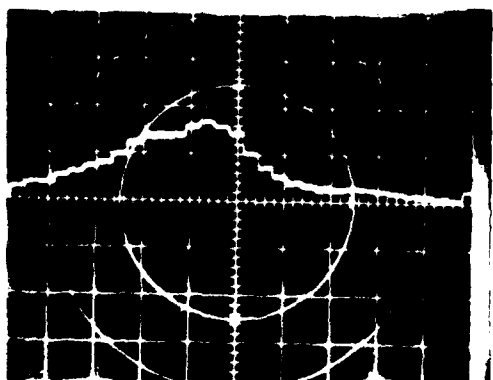
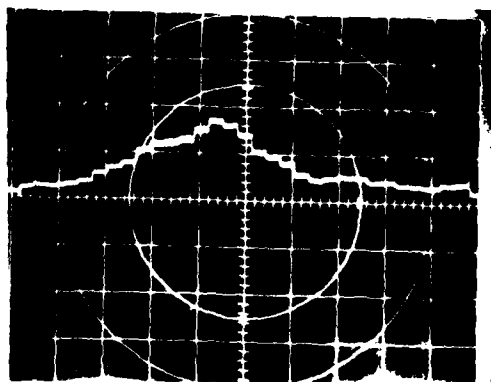
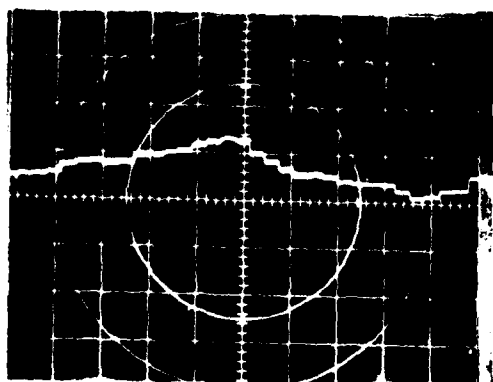
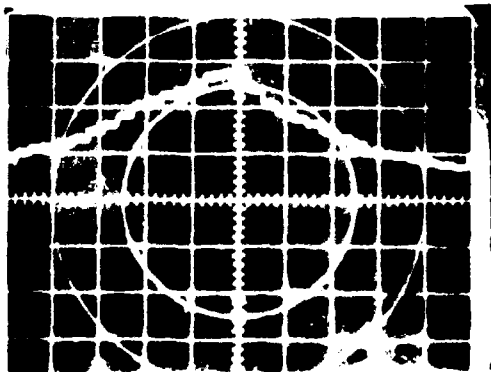
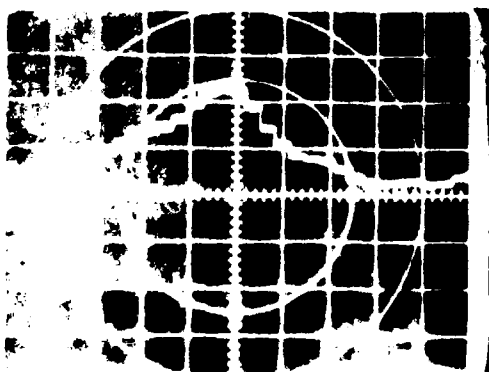
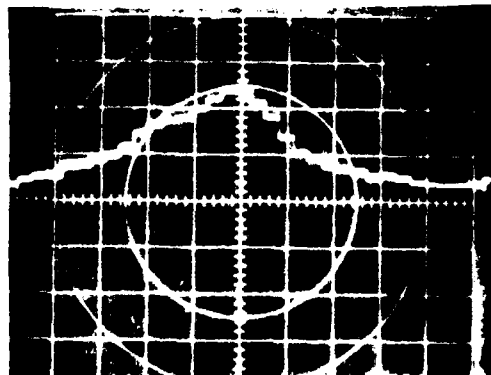
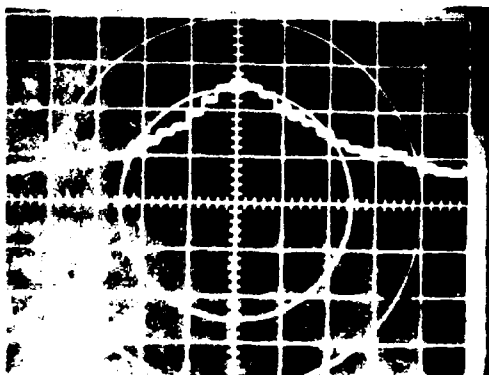
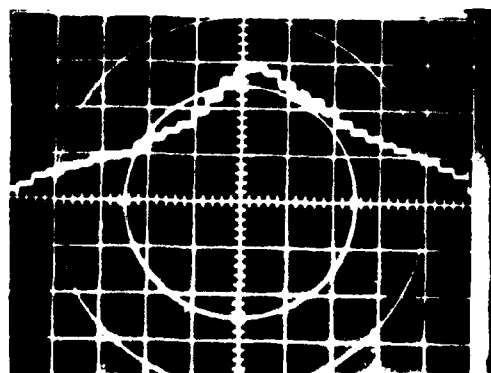
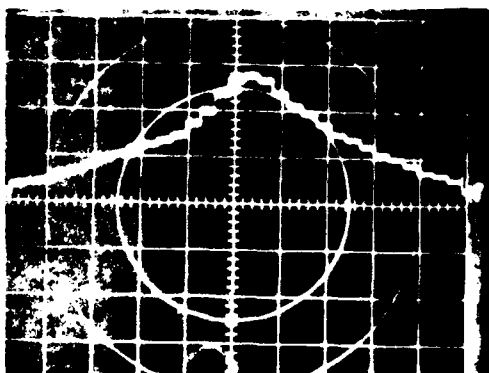
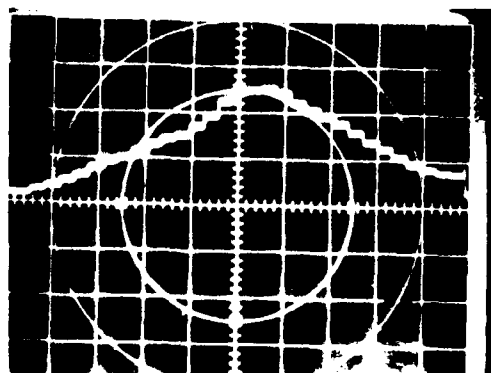
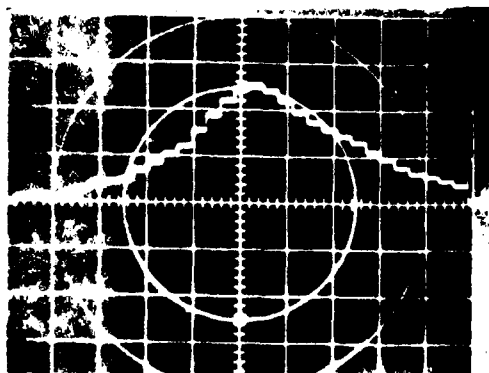


Figure 1. Comparison of the results of the 118 data starting 11:25 February 14, 1979, with the results of the 118 data starting 11:25 February 14, 1979, with the results of the 118 data starting 11:25 February 14, 1979.



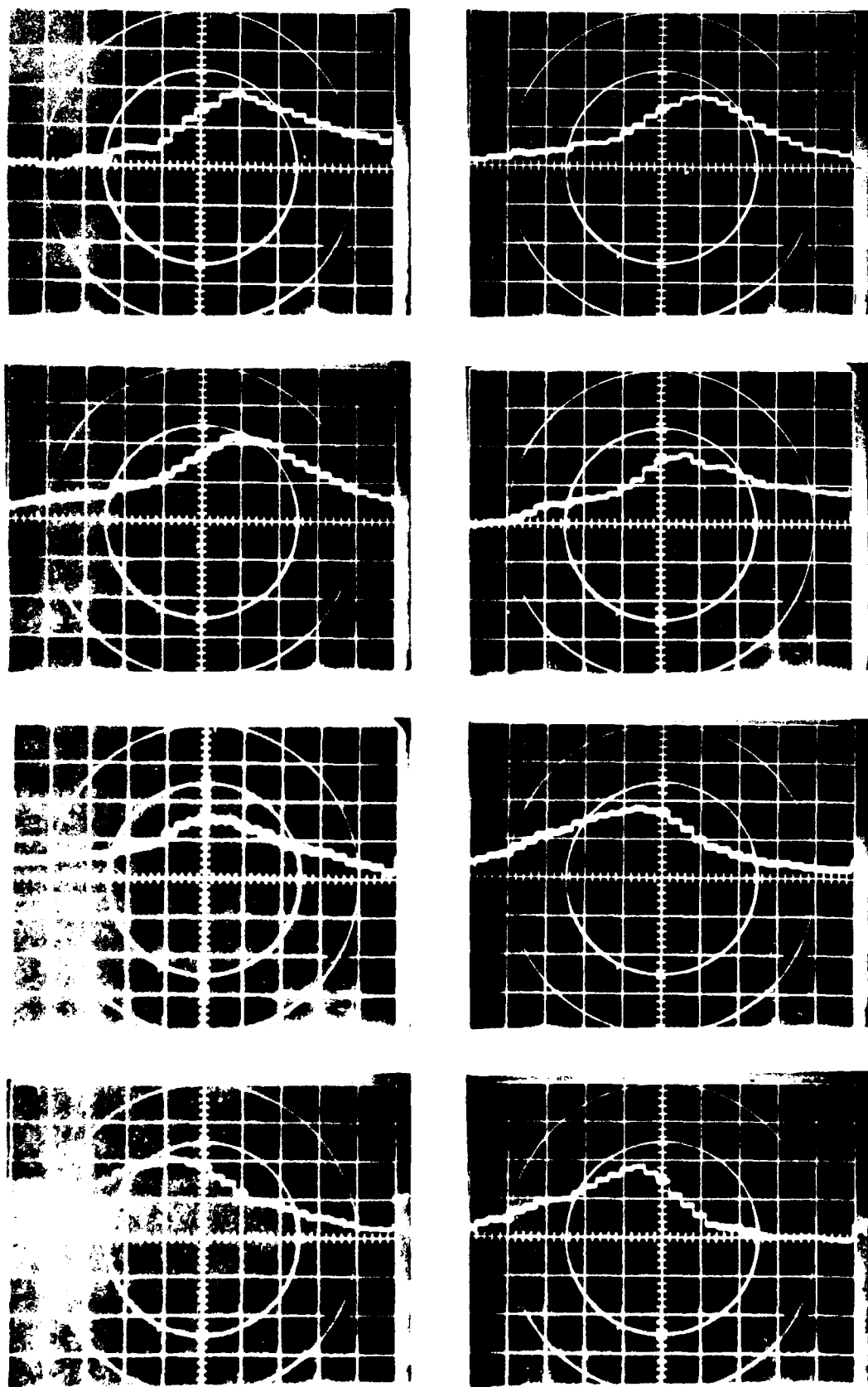


Figure 15. Covariance functions from FLIR data starting 1108 February 14, 1979.
 The view is just grazing the top of Table Mountain. C_n^2 is 3 to $6 \times 10^{-13} \text{ m}^{-2/3}$.
 The delay is 4000000 ft and the sample interval is 50 ft.

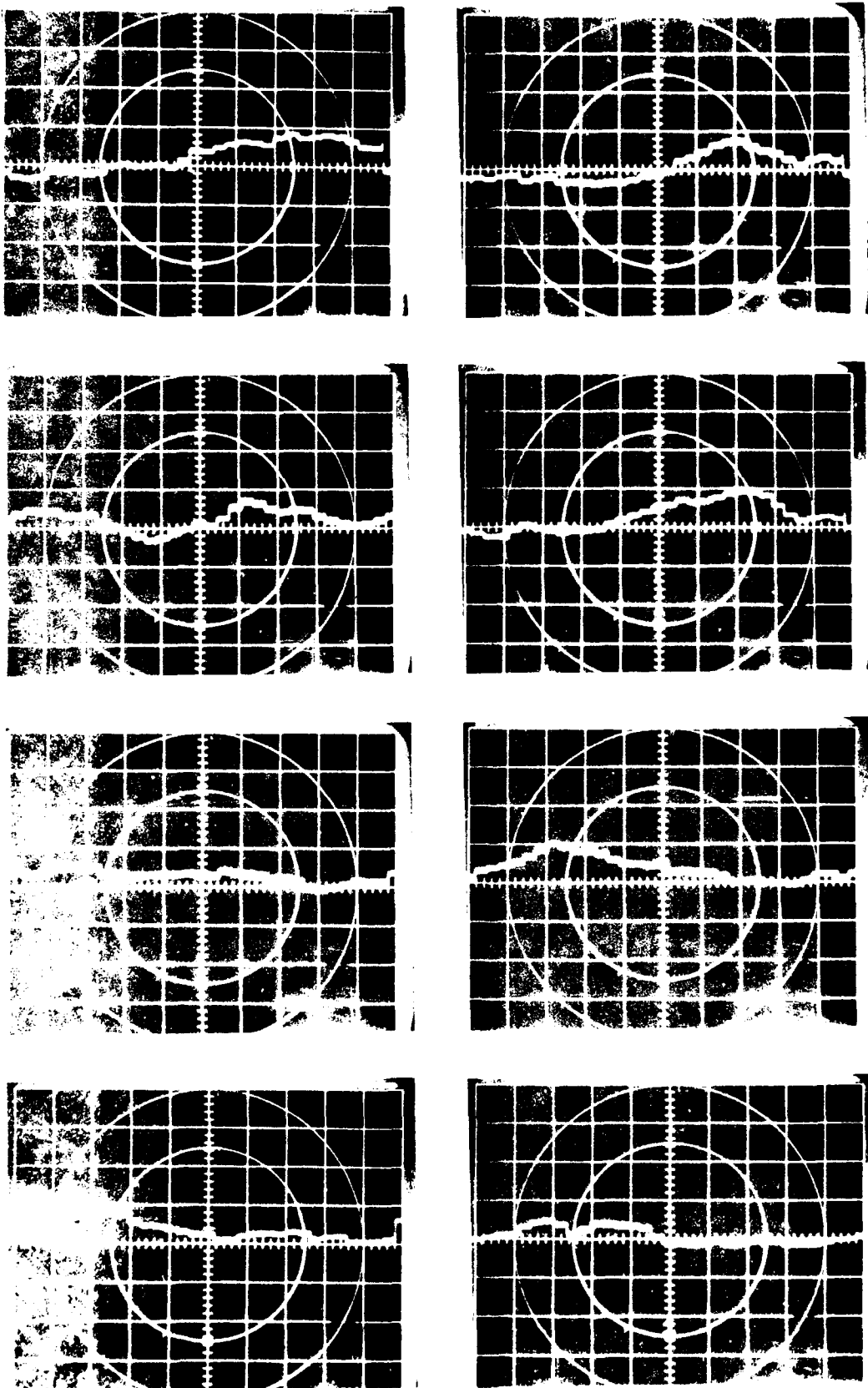


Figure 16. Covariance functions from FLIR data starting 1108 February 14, 1979.
 The view is just grazing the top of Table Mountain. C_n^2 is 3 to $6 \times 10^{-13} \text{ m}^{-2/3}$.
 The delay is 60 ms per bit and the sample interval is 200 ns.

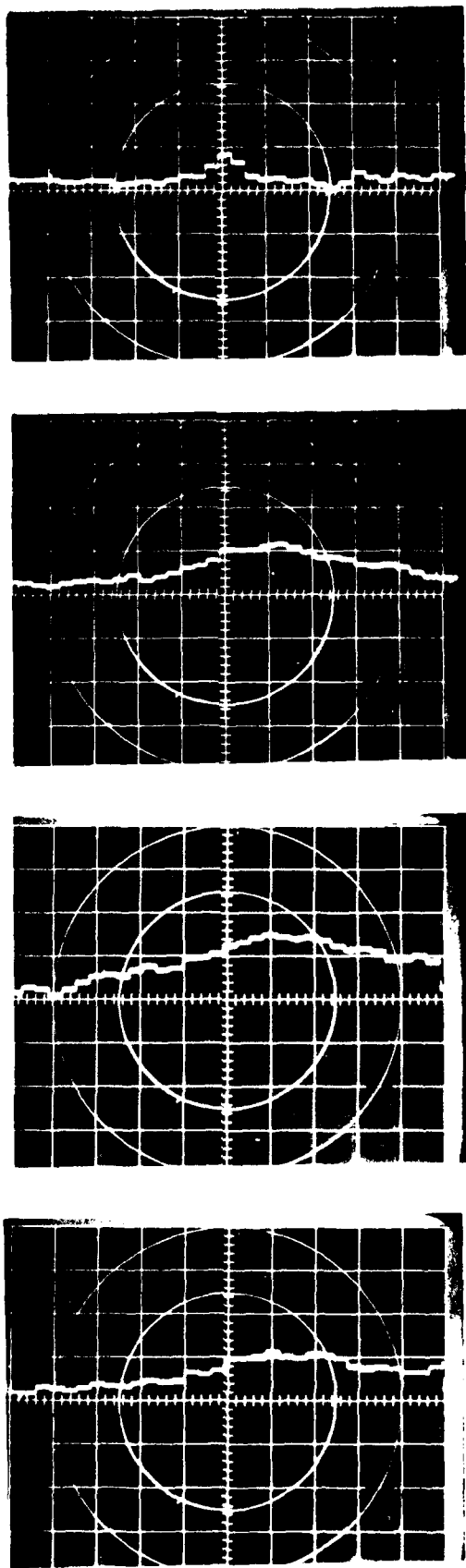


Figure 17. Covariance functions from FLIR data. The top function was taken at 0940 February 14, 1979 during a light snow. The remaining functions were taken on the night of February 14, beginning at 2100, when C_n^2 was $4-8 \times 10^{-14} \text{ m}^{-2/3}$. The delay is 30 ms per bit and the sample interval is 100 μs .

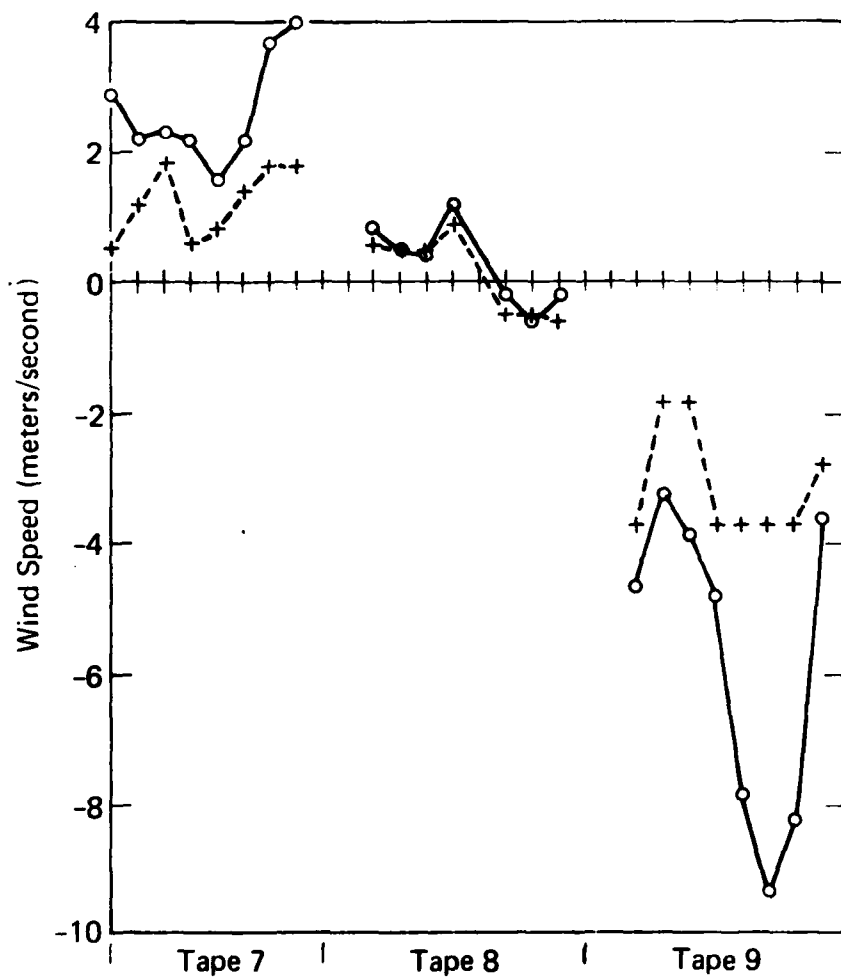


Figure 18. FLIR derived wind speeds compared with the average of 5 propeller anemometers along the optical path. The FLIR cannot read the higher wind speeds correctly because of the limitation imposed by the sweep rate.

The upper covariance function shown in Fig. 17 was obtained when it was snowing lightly. Very likely the peak on the function at zero time delay results from snow flakes going through the field of view near the receiver since snow flakes farther away would result in little signal fluctuation and even less correlation between signal fluctuations in the two detectors. The remaining three covariance functions of Fig. 17 were obtained at night. C_n^2 was 4 to 8×10^{-14} and apparently there was sufficiently different irradiance within the scene at $10 \mu\text{m}$ wavelength so that performance was similar to daytime operation.

4. CONCLUSIONS AND RECOMMENDATIONS

It is possible to measure horizontal crosswinds by processing the video signals available in the FLIR thermal sight. The measurement can only be made, however, under very restrictive conditions. These conditions are as follows:

1. C_n^2 greater than about $1 \times 10^{-14} \text{ m}^{-2/3}$

It is unlikely that a passive wind measuring system can ever be expected to operate in all weather conditions. C_n^2 will vary at least over four orders of magnitude near the ground. While active optical wind measurement systems almost never encounter so small a value of C_n^2 that operation is not possible, a passive system does because it relies upon sufficient ambient radiation from the scene, and contrast of details within the field of view. In addition, passive wind sensors operating in the $10 \mu\text{m}$ region have S/N ratios which are about two orders of magnitude less than a visual system.

2. Sufficient contrast of the right kind in the image

In a passive wind sensor, both the reflected light and C_n^2 tend to decrease at the same time and the multiplicative effect may result in insufficient

S/N. In the $10\text{ }\mu\text{m}$ wavelength region, a passive system detects differences in radiation, which are largely due to temperature differences. Again, C_n^2 tends to be small at the same time that the temperature differences are small, and the multiplicative effect results at times in insufficient S/N. An additional problem exists in that both detectors in the focal plane must see scenes having suitable and very similar spatial spectra. For example a view of the horizon, bisecting the fields of view of both detectors, is ideal. But if the detectors observe just above or below the horizon, or if one detector sees the horizon and the other one does not, the system may not work at all. In principle, one might have a computer scan the scene and find those horizontally spaced, adjacent pairs of points which both display high signal fluctuation levels. This is, of course, what was done manually to obtain suitable locations in the focal plane from which we obtained the experimental results shown in the previous section. However, not all locations selected in this way are useful, presumably because the two detectors see different scene spectra.

3. Thermal sight stationary

Motion of the receiver affects a focal plane system to a far greater extent than passive systems which observe the intensity scintillation pattern at two locations at the receiver. These systems have both much larger angular fields of view and nearly coincident fields of view, so that both detectors observe the same scene. In general, angular motion of the larger field of view produces less signal modulation, and of course the changes are the same for both apertures. Both the slope and the covariances have only a second order response to simultaneous fluctuations in both apertures, mainly resulting in a reduction in S/N. For focal plane image measurements, the FLIR sight in fact had a noticeable vibration from its cooling unit as originally set up and it was necessary to use wood blocks to damp it out.

4. Thermal sight image in exact focus

All of the experimental results are dependent upon the detectors being placed exactly in the image plane. A quite different calibration and wind weighting function will be obtained if the detectors are inside or outside of focus. In fact, if they are outside of focus the indicated direction of the wind will be reversed. Since the FLIR sensor is focused manually, there is no assurance of exact focus.

5. Wind less than 4 m/s

The sweep rate of the thermal sight inherently limits the wind speed that can be observed. While the limit was about 2 m/s in the present experiment, this was due to the tape recorder bandwidth; about 4 m/s should be possible.

There is an alternate way of making the crosswind measurement. By inserting two new detectors inside the focus of the present thermal sight (probably using a beam splitter) it would be possible to operate on the principle of separate receiving apertures as used in the earlier passive systems operating at visual wavelengths. A 1 kHz bandwidth would be adequate for 30 m/s winds, and better S/N would result from the reduced bandwidth and continuous sampling. This arrangement would eliminate the focus problem and reduce, though not eliminate, the problem of image motion and variation in the scene spectrum. The C_n^2 level requirement will remain essentially the same.

In summary, it is clearly possible under laboratory conditions to use the infrared image to obtain crosswind information day or night when C_n^2 is high enough and the scene is suitable (for example looking at the horizon sharply defined against a cold sky). Exact focusing requirements, vibration and movement problems, and other unfavorable characteristics inherent in using information gathered in the image plane appear to make

this technique unsatisfactory for obtaining routine crosswind information. Modifying the original thermal sight by adding several detectors inside the focal plane eliminates the focus problem and reduces some of the other difficulties. Even with a stationary platform, however, the modified system could not be expected to operate all of the time that the thermal sight can produce images.

5. REFERENCES

1. Ochs, G. R., and Ting-i Wang, 1977, Infrared Passive Wind Sensing - A Feasibility Study, NOAA Technical Memorandum, ERL WPL-34.
2. Lutomirski, R. F., and H. T. Yura, 1971, "Propagation of a Finite Optical Beam in an Inhomogeneous Medium," Appl Opt, 10:1652.
3. Tatarski, V. I., 1961, Wave Propagation in a Turbulent Medium, McGraw-Hill, New York.
4. Tatarski, V. I., 1971, The Effects of the Turbulent Atmosphere on Wave Propagation, National Technical Information Service, Springfield, VA.
5. Lawrence, R. S., G. R. Ochs, and S. F. Clifford, 1972, "Use of Scintillations to Measure Average Wind Across a Light Beam," Appl Opt, 11:239.
6. Lee, M. H., J. F. Holmes, and J. Richard Kerr, 1976, "Statistics of Speckle Propagation through the Turbulent Atmosphere," J Opt Soc Am, 66:1164.
7. Lee, M. H., J. F. Holmes, and J. R. Kerr, 1977, "Generalized Spherical Wave Coherence Function," J Opt Soc Am, 67, 1279.
8. Wang, Ting-i, S. F. Clifford, and G. R. Ochs, 1974, "Wind and Refractive Turbulence Sensing Using Crossed Laser Beams," Appl Opt, 13:2602.
9. Clifford, S. F., G. R. Ochs, and Ting-i Wang, 1975, "Optical Wind Sensing by Observing the Scintillations of a Random Scene," Appl Opt, 14:2844.
10. Ochs, G. R., W. D. Cartwright, and P. S. Endow, 1979, Optical System Model III for Space-Averaged Wind Measurements, NOAA Technical Memorandum ERL-WPL-46.
11. FLIR Common Module Design Manual, OR 14, 118, revised 1 March 1978, Martin Marietta Corporation, Orlando, Florida 32855.
12. Direct Support and General Support Maintenance for Sight, Thermal, Tank-Mounted AN/ASG-2, September 1977, Department of the Army Technical Manual, DEP TM 11-5855-248-34.